

# In Situ Formed “Sn<sub>1-x</sub>In<sub>x</sub>@In<sub>1-y</sub>Sn<sub>y</sub>O<sub>z</sub>” Core@Shell Nanoparticles as Electrocatalysts for CO<sub>2</sub> Reduction to Formate

Laura C. Pardo Pérez, Detre Teschner, Elena Willinger, Amandine Guiet, Matthias Driess, Peter Strasser, and Anna Fischer\*

Electrochemical reduction of CO<sub>2</sub> (CO<sub>2</sub>RR) driven by renewable energy has gained increasing attention for sustainable production of chemicals and fuels. Catalyst design to overcome large overpotentials and poor product selectivity remains however challenging. Sn/SnOx and In/InOx composites have been reported active for CO<sub>2</sub>RR with high selectivity toward formate formation. In this work, the CO<sub>2</sub>RR activity and selectivity of metal/metal oxide composite nanoparticles formed by in situ reduction of bimetallic amorphous SnInOx thin films are investigated. It is shown that during CO<sub>2</sub>RR the amorphous SnInOx pre-catalyst thin films are reduced in situ into Sn<sub>1-x</sub>In<sub>x</sub>@In<sub>1-y</sub>Sn<sub>y</sub>O<sub>z</sub> core@shell nanoparticles composed of Sn-rich SnIn alloy nanocores (with  $x < 0.2$ ) surrounded by InOx-rich bimetallic InSnOx shells (with  $0.3 < y < 0.4$  and  $z \approx 1$ ). The in situ formed particles catalyze the CO<sub>2</sub>RR to formate with high faradaic efficiency (80%) and outstanding formate mass activity (437 A g<sub>In+Sn</sub><sup>-1</sup> @ -1.0 V vs RHE in 0.1 M KHCO<sub>3</sub>). While extensive structural investigation during CO<sub>2</sub>RR reveals pronounced dynamics in terms of particle size, the core@shell structure is observed for the different electrolysis conditions essayed, with high surface oxide contents favoring formate over hydrogen selectivity.

CO<sub>2</sub> atmospheric concentrations.<sup>[4-6]</sup> In this context, the electrochemical conversion of CO<sub>2</sub> into fuels driven by a renewable energy input has attracted increasing attention as a promising approach to chemically store renewable energy in C-based fuels. Electrochemical reduction of CO<sub>2</sub> allows converting CO<sub>2</sub> in fuels under mild chemical conditions, such as aqueous media and ambient temperature and pressure. However, energy efficiency remains elusive as overpotentials as large as 1 V are required to bring the process to a desired production rate.


The CO<sub>2</sub> reduction reaction, abbreviated as CO<sub>2</sub>RR, is a complex process that requires multiple electron and proton transfer reactions which can lead to a wide variety of products including CO,<sup>[7-14]</sup> HCOOH,<sup>[7,10,11,13,15-17]</sup> hydrocarbons (mainly methane and ethylene),<sup>[13,14,18-21]</sup> or CH<sub>3</sub>OH.<sup>[22-26]</sup> In aqueous medium CO<sub>2</sub>RR is in competition with H<sub>2</sub> evolu-

tion (HER). Accordingly, selectivity control in CO<sub>2</sub>RR is a major challenge. Early studies of CO<sub>2</sub> electroreduction in aqueous media were primarily focused on electrode materials with a large HER overpotential such as Hg.<sup>[27-31]</sup> In addition, the pioneering work of Hori,<sup>[9,14]</sup> Vassiliev,<sup>[32]</sup> and further contributions of Azuma<sup>[7]</sup> and Ito<sup>[10,13]</sup> provided a large pool of experimental

## 1. Introduction

The exhaustive use of carbon-based fossil fuels has led to a pronounced increase of CO<sub>2</sub> emissions over the past century.<sup>[1-3]</sup> The environmental impact of these emissions has drawn attention to the necessity to stabilize and eventually decrease the

L. C. Pardo Pérez,<sup>[†]</sup> A. Guiet,<sup>[††]</sup> M. Driess, A. Fischer  
Institute of Chemistry—Inorganic Chemistry  
Technical University Berlin  
Straße des 17. Juni 135, 10623 Berlin, Germany  
E-mail: anna.fischer@ac.uni-freiburg.de

 The ORCID identification number(s) for the author(s) of this article can be found under <https://doi.org/10.1002/adfm.202103601>.

© 2021 The Authors. Advanced Functional Materials published by Wiley-VCH GmbH. This is an open access article under the terms of the Creative Commons Attribution License, which permits use, distribution and reproduction in any medium, provided the original work is properly cited.

<sup>[†]</sup>Present address: Electrochemical Conversion of CO<sub>2</sub> group, Helmholtz-Zentrum Berlin für Materialien und Energie, Hahn-Meitner-Platz 1, 14109 Berlin, Germany

<sup>[††]</sup>Present address: Institut des Molécules et Matériaux du Mans (IMMM), UMR 6283 CNRS, Le Mans Université, Avenue Olivier Messiaen, Le Mans Cedex 9 72085, France

DOI: 10.1002/adfm.202103601

L. C. Pardo Pérez, A. Fischer  
Institute of Inorganic and Analytical Chemistry  
University of Freiburg  
Albertstraße 21, 79104 Freiburg, Germany

D. Teschner, E. Willinger  
Department of Inorganic Chemistry  
Fritz-Haber-Institute der Max-Planck-Gesellschaft  
Faradayweg 4–6, 14195 Berlin, Germany

D. Teschner  
Department of Heterogeneous Reactions  
Max-Planck-Institute for Chemical Energy Conversion  
Stiftstraße 34–36, 45470 Mülheim an der Ruhr, Germany

P. Strasser  
Institute of Chemistry—Technical Chemistry  
Technical University Berlin  
Straße des 17. Juni 124, 10623 Berlin, Germany

A. Fischer  
FMF—Freiburger Materialforschungszentrum  
University of Freiburg  
Stefan-Meier-Straße 21, 79104 Freiburg im Breisgau, Germany

results for CO<sub>2</sub> reduction on various metal electrodes. The metals have been empirically classified according to the major CO<sub>2</sub>RR reduction product in aqueous media. While metals like Pt were found to have negligible activity for CO<sub>2</sub>RR, Ag and Au were found to favor the production of CO. Interestingly, Cu was found to catalyze the production of higher reduction products such as hydrocarbons. In contrast, metallic Sn and In electrodes have been found to catalyze the conversion of CO<sub>2</sub> preferentially to formate (HCOO<sup>-</sup>).<sup>[7,9,10,13,14,32]</sup>

Formic acid or formate salts have multiple possible applications as building blocks for re-utilization of CO<sub>2</sub>. They can be used as direct fuel in direct formic acid fuel cells (DFAFC), potentially offering a CO<sub>2</sub> neutral fuel cycle, as hydrogen storage vector or as raw material in industry.<sup>[33–35]</sup> However so far, the reported faradaic efficiencies offered by metallic Sn<sup>[36]</sup> and In catalysts<sup>[37]</sup> (in potential windows between –1.0 V to –1.5 V vs RHE) vary significantly among reports<sup>[7,9,43–49,13,16,17,38–42]</sup> At applied potentials around –1.0 V versus RHE, Sn and In were found to provide formate faradaic efficiencies between 63–88% and 69–95% respectively, while at larger reductive bias, that is, in the range of –1.3 to –1.5 V versus RHE, the production of H<sub>2</sub> is favored, thereby decreasing the faradaic efficiency for formate to only 5.2% and 33.3% for Sn and In respectively.<sup>[7]</sup>

Recent reports have pointed out that the origin of the variability of formate faradaic efficiencies reported on Sn and In based catalysts could be associated with the native oxide layer present at the surface of these metals. For instance, Kanan reported that at low applied potential of –0.7 V versus RHE, a tin foil with a native oxide layer exhibits a formate faradaic efficiency of about 19%, while a freshly acid-etched foil, without a native oxide layer virtually produced no formate, as indicated by the extremely low value of 0.3% of the formate faradaic efficiency.<sup>[38]</sup> To gain further understanding on the influence of SnOx surface oxide species on the activation of CO<sub>2</sub> to formate, the authors also reported the simultaneous electrodeposition of Sn<sup>0</sup> and SnOx (SnOx/Sn<sup>0</sup>) on a titanium foil, during CO<sub>2</sub> electrolysis experiments at –0.7 V versus RHE. A CO<sub>2</sub> conversion faradaic efficiency of 85–98% (Formate 40% + CO 58%) was thereby found. The high selectivity toward CO<sub>2</sub> conversion into CO and HCOO<sup>-</sup> over HER on these electrodes strongly suggests a boost of CO<sub>2</sub> conversion over H<sub>2</sub> evolution due to the presence of surface oxides (of the type SnOx). However, the electrodeposited SnOx/Sn<sup>0</sup> composite tends to lose its conductivity upon contact with air and consequently its activity.

A study on a hierarchical dendrite Sn structure electrodeposited on a tin foil<sup>[39]</sup> revealed that the high surface area structure could deliver higher current densities and that increasing the oxygen content in the material's surface through heat treatment in air led to significant improvement in the formate faradaic efficiency (from 32% to 55.9% at –1.06 V vs RHE). A step further in the investigation of the role of SnOx moieties on the CO<sub>2</sub>RR electrocatalytic activity was proposed by Meyers group,<sup>[40]</sup> who reported in situ electrochemically reduced tin oxide nanoparticles capable of catalyzing the conversion of CO<sub>2</sub> into formate in NaHCO<sub>3</sub> aqueous solutions with faradaic efficiencies as high as 86.2% at –1.2 V versus RHE.

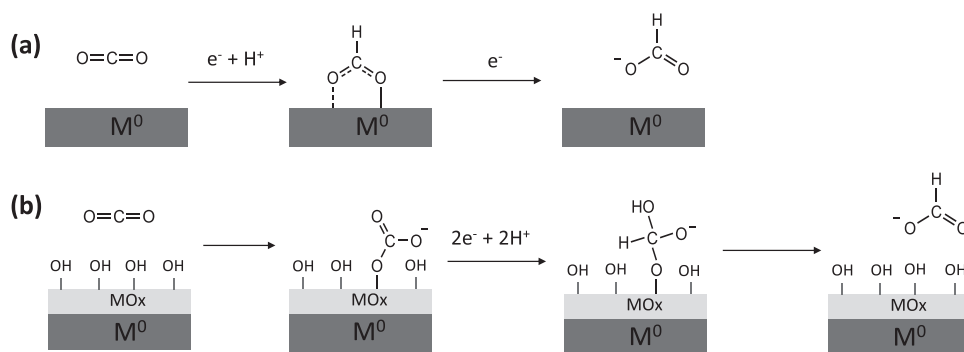
An analogous behavior was reported on Indium surfaces. Bocarsly's group reported that Indium electrodes with a native oxide layer could provide up to 75% faradaic efficiency for

formate formation at –0.9 V versus RHE. However, the stability was limited, as over 2 h of operation, the faradaic efficiency for formate dropped below 20%; a value typically obtained for freshly acid-etched In electrodes. Anodized In electrodes provided a stable faradaic efficiency of 35–40% over 6 h.<sup>[41]</sup> The same group reported a comparative study of the activity of In(OH)<sub>3</sub>, In<sub>2</sub>O<sub>3</sub> and metallic In nanoparticles.<sup>[42]</sup> High faradaic efficiencies (>70%) could be reached with these catalysts at moderate applied potentials (–0.9 to –1.2 V vs RHE). Interestingly, In<sup>0</sup> NP's with native In–OH and In–O surface species were found to provide virtually 100% faradaic efficiency toward formate, while pure In(OH)<sub>3</sub> and In<sub>2</sub>O<sub>3</sub> nanoparticles reached lower faradaic efficiencies and required larger overpotentials, probably due to their lower conductivity, when compared to the metallic nanoparticles.

In regard of the mechanisms of formate production on Sn- and In-based catalysts two possible pathways have been proposed. Correlation of experimentally observed partial current densities and theoretical insights on intermediates binding strength indicate that the production of formate on metal surfaces proceeds through an oxygen bound intermediate \*OCHO<sup>[50]</sup> as depicted in **Scheme 1a**. ATR-IR studies on the effect of surface oxidized species of the types MOx in Sn- and In-based catalysts<sup>[41,43]</sup> indicate an alternative mechanism. These studies conclude that the presence of an oxide layer on Sn and In surfaces leads to the formation of hydroxylated surfaces (M–OH) in aqueous media that react with dissolved CO<sub>2</sub> to form an adsorbed carbonate (M–CO<sub>3</sub><sup>-</sup>) intermediate that is proposed to undergo a two-electron reduction to yield formate as depicted in **Scheme 1b**. The mechanism proceeding through an M–CO<sub>3</sub><sup>-</sup> was also found viable by DFT studies conducted on hydroxyl terminated SnO surfaces.<sup>[51]</sup> The proposed mechanisms implicate the persistence of SnOx or InOx surface species at potentials relevant for CO<sub>2</sub>RR. A recent investigation on SnO<sub>2</sub> nanoparticles (4 nm) supported on graphene by in situ Raman spectroscopy and XAS<sup>[52]</sup> revealed that SnO<sub>2</sub> and SnO surface moieties persist at the catalyst surface in the potential range where the best formate faradaic efficiency is observed (–0.8 V vs RHE in KHCO<sub>3</sub> pH 8.5); providing further evidence that persistent oxides play a key role in CO<sub>2</sub>RR.

To summarize, Indium has been consistently found to provide higher faradaic efficiencies at larger overpotentials than Tin.<sup>[7,9,13,16,17,40–43]</sup> For both electrode materials, recent reports point out that MOx enriched surfaces (with M being In or Sn) or M<sup>0</sup>/MOx composites both boost the faradaic efficiency toward formate. However, in view of the overall system conductivity, a compromise must be met between the amount of metal and metal oxide to preserve the material's high conductivity.<sup>[38,42]</sup>

In this context, amorphous bimetallic indium tin oxide thin films (SnInOx)<sup>[53–56]</sup> appear as an interesting class of material for CO<sub>2</sub>RR electrocatalysis. Such amorphous yet conductive SnInOx thin films enable the investigation of possible synergies between Sn and In for the electrocatalytic conversion of CO<sub>2</sub> to formate, while simultaneously providing an oxygen-rich matrix for the formation of stable metal oxide surface species (such as InOx and/or SnOx), known to favor the production of formate with high faradaic efficiency. In the present paper, the study of amorphous SnInOx thin films as (pre)electrocatalysts for oxide-derived CO<sub>2</sub>RR reduction catalysts as well as a detailed



**Scheme 1.** Mechanisms of formate production for In- or Sn-based catalysts proposed in literature: a) Production of formate via  $^*OCHO$  intermediate,<sup>[50]</sup> b) Production of formate via  $M-CO_3^-$  intermediate.<sup>[41,43]</sup> Note: M corresponds to Sn or In and  $MO_x$  refers to surface oxide species on these metal surfaces.

investigation of their activity toward  $CO_2$  reduction along with in-depth insights into material reduction and restructuring upon  $CO_2RR$  reaction are presented.

Our results revealed that  $SnInO_x$  thin films act as pre-catalysts for the in situ formation under  $CO_2$  electroreduction conditions of metal@metal oxide core@shell nanoparticles, composed of Sn-rich  $Sn_{1-x}In_x$  alloyed nanocores (with  $x < 0.2$ ) surrounded by InOx-rich bimetallic  $In_{1-y}Sn_yO_z$  shells (with  $0.3 < y < 0.4$  and  $z \approx 1$ ). The investigation of these in situ formed nanoparticles under diverse applied electrolysis potentials and extended electrolysis time revealed a dynamic particle size evolution during  $CO_2RR$ . Interestingly, despite the particle size changes the “ $Sn_{1-x}In_x@In_{1-y}Sn_yO_z$ ” core@shell structures with a  $\approx 3$  nm oxide surface layer were found to be intrinsically favored in all conditions essayed. Similar In surface segregation in form of  $In(OH)_3$  has been previously observed under  $CO_2RR$  conditions for bimetallic Cu–In catalysts.<sup>[57]</sup> Such core@shell structures offer potential advantages for electrocatalysis. For instance, they maximize the exposition of the shell component to the electrolyte as has been used to increase utilization of precious metals for ORR application.<sup>[58,59]</sup> They can also offer the possibility of tuning  $CO_2R$  selectivity through cooperation between core and shell components as has been demonstrated for  $Ag@SnO_x$ <sup>[60,61]</sup> and  $Cu@In(OH)_3$ <sup>[57]</sup> catalysts for  $CO_2RR$ .

## 2. Results and Discussion

Amorphous  $SnInO_x$  thin films with a film thickness of 20–25 nm were deposited onto glassy carbon plate-like substrates by spin coating using a single source precursor approach (for details see experimental part as well as HR-SEM and TEM images in Figure S1, Supporting Information). The composition of the as-obtained  $SnInO_x$  thin films was investigated by energy dispersive x-ray spectroscopy (EDX), induced coupled plasma-optical emission spectroscopy (ICP-OES), and x-ray photoelectron spectroscopy (XPS), revealing an average In:Sn ratio of 0.4 (Table 1). The  $CO_2RR$  electrocatalytic activity of the  $SnInO_x$  film was evaluated in a two-compartment cell provided with a constant inlet of  $CO_2$  at  $30 \text{ mL min}^{-1}$  using  $CO_2$  saturated 0.1 M  $KHCO_3$  (pH 6.8) as an electrolyte. A fritted tube was used to separate the counter electrode to prevent re-oxidation of  $CO_2RR$  products. Further details can be found in the experimental

section and supporting information (Figure S2a, Supporting Information). The electrolysis experiment comprised a linear sweep voltammetry (LSV) in the reductive direction from +0.4 V to  $-1.0$  V versus RHE followed by a chronoamperometry at  $-1.0$  V versus RHE for 10 min. The gaseous products such as  $H_2$  and CO were analyzed by gas chromatography, while the products in the liquid phase were analyzed by  $^1H$ -NMR.

In the cathodic LSV in  $CO_2$  saturated electrolyte, the  $SnInO_x$  films exhibit an intrinsic reduction peak at  $-0.58$  V versus RHE, which appears to overlap with the onset of  $CO_2RR$  and corresponds to the reduction of bimetallic  $SnInO_x$  to the respective metallic form (Figure 1a and inset in Figure 1a). The overall catalytic current reaches  $-78 \text{ mA cm}^{-2}$  at  $-1.0$  V versus RHE. During the chronoamperometry step, the current decays within the first minutes and stabilizes at  $-6.4 \text{ mA cm}^{-2}$  (Figure 1b). The product analysis revealed that the main  $CO_2$  reduction product is formate with a faradaic efficiency of 80%. Additionally, CO was produced with a faradaic efficiency of 5.4%, while  $H_2$  was produced with a faradaic efficiency of 14.5% (Figure 1c).

For comparison, a cathodic LSV was performed for an  $SnInO_x$  film in  $CO_2$ -free,  $N_2$ -saturated electrolyte. Under these conditions, only HER is expected. During the LSV the  $SnInO_x$  intrinsic reduction peak appears at  $-0.54$  V versus RHE (Figure 1a). The catalytic current sets on at lower potential ( $-0.65$  V vs RHE) than it was observed in the presence of  $CO_2$  and reaches  $-5.2 \text{ mA cm}^{-2}$  at  $-1.0$  V versus RHE, while decaying to  $-3.7 \text{ mA cm}^{-2}$  during the 10 min chronoamperometry test. The product analysis revealed, as expected, the sole production of  $H_2$  with 100% faradaic efficiency (Figure 1c).

The electrolysis experiments conducted in both  $N_2$  and  $CO_2$  saturated electrolytes (Figure 1a) revealed that both  $CO_2$  reduction and  $H_2$  evolution onset after the electrochemical reduction of the  $SnInO_x$  films. The extent of  $SnInO_x$  film reduction will be discussed in detail in the next section (vide infra). In short, TEM and SEM characterization revealed that the amorphous  $SnInO_x$  thin films act as precatalysts and are reduced in situ during the  $CO_2RR$  reaction to form core@shell nanoparticles composed of Sn-rich metallic alloy cores of the type  $Sn_{1-x}In_x$  ( $x < 0.2$ ) surrounded by indium-rich indium tin oxide shells of the type  $In_{1-y}Sn_yO_z$  with  $y = 0.4$  and  $z \approx 1$ , denoted “ $Sn_{1-x}In_x@In_{1-y}Sn_yO_z$ ”core@shell in the following.

It is important to note that HER activity is heavily suppressed in  $CO_2$  saturated electrolyte for these  $SnInO_x$ -derived

**Table 1.** Composition of as synthesized SnInOx films and in situ formed “Sn<sub>1-x</sub>In<sub>x</sub>@In<sub>1-y</sub>Sn<sub>y</sub>O<sub>z</sub>” core@shell nanoparticles during CO<sub>2</sub> reduction determined by different analytical methods (ICP, EDX, XPS).

	Technique	Sn <sup>a)</sup>	In <sup>a)</sup>	O/M <sup>b)</sup>	In:Sn
As synthesized SnInOx films	ICP	0.69	0.31	–	0.44
	SEM-EDX <sup>c)</sup>	0.71	0.29	1.5	0.40
	XPS (500 eV) <sup>c)</sup>	0.78	0.22	2.0	0.29
Sn <sub>1-x</sub> In <sub>x</sub> @In <sub>1-y</sub> Sn <sub>y</sub> O <sub>z</sub> core@shell nanoparticles in SnInO <sub>x</sub> -CAT@-1V_10min	ICP (bulk)	0.63	0.37	–	0.58
	SEM-EDX (bulk) <sup>c)</sup>	0.63	0.37	3.3-6.3	0.59
	STEM <sup>c)</sup> Core	0.85	0.15	0.4	0.18
	Shell	0.14	0.86	1.9	6.05
	XPS <sup>d)</sup> 200 eV	0.42	0.58	–	1.33
	500 eV	0.45	0.55	1.1	1.23
	1000 eV	0.48	0.52	–	1.10
	XPS <sup>c)</sup> 500 eV	0.42	0.58	1.7	1.39

<sup>a)</sup>Sn and In fraction referred to the total metal content; Sn = at%Sn/(at%Sn + at%In); <sup>b)</sup>Oxygen to total metal ratio O/M = at%O/(at%Sn + at%In); <sup>c)</sup>Characterization conducted on samples exposed to air; <sup>d)</sup>\* denotes characterization conducted on samples handled, stored, and transferred under inert atmosphere.

nanoparticle films (Figure 1b,c). Indeed, in situ reduced SnInOx provides a partial HER catalytic current density of  $-3.7 \text{ mA cm}^{-2}$  in N<sub>2</sub> saturated electrolyte and a 100% faradaic efficiency toward H<sub>2</sub> evolution. However, in CO<sub>2</sub> saturated electrolyte, the faradaic efficiency for H<sub>2</sub> evolution drops down to 14.5% accounting for a H<sub>2</sub> partial current of only  $-0.92 \text{ mA cm}^{-2}$ . These results indicate that although the in situ reduced SnInOx does catalyze H<sub>2</sub> evolution, in the presence of CO<sub>2</sub> it exhibits a marked affinity and higher activity toward the activation of CO<sub>2</sub>.

The affinity of the SnInOx derived composites for CO<sub>2</sub> can further be observed by comparing the reduction of SnInOx in N<sub>2</sub> and CO<sub>2</sub> saturated electrolyte by voltammetry (Figure 1a,d). The inset in Figure 1a displays the redox peaks observed upon the reduction of SnInOx films in the first cathodic sweep in N<sub>2</sub> and CO<sub>2</sub> saturated electrolyte, respectively. In N<sub>2</sub>-saturated electrolyte, a sharp reduction peak ascribed to the reduction of InO<sub>x</sub> (In<sup>δ+</sup>) to metallic In<sup>0</sup> and SnO<sub>x</sub> (Sn<sup>δ+</sup>) to metallic Sn<sup>0</sup> is observed at  $-0.54 \text{ V}$ , while the onset of hydrogen evolution current is observed at higher reductive bias. In the presence of CO<sub>2</sub> however, the redox peak located at  $-0.58 \text{ V}$  is less sharp and overlaps with the onset of CO<sub>2</sub> reduction current. It is during this first reduction sweep that the SnInOx film is transformed into “Sn<sub>1-x</sub>In<sub>x</sub>@In<sub>1-y</sub>Sn<sub>y</sub>O<sub>z</sub>” core@shell nanoparticles. Figure 1d displays a stable CV profile in N<sub>2</sub> and CO<sub>2</sub> saturated electrolyte after 5 cycles at  $100 \text{ mV s}^{-1}$ . While the redox peaks associated to the InSnOx reduction are still clearly seen in N<sub>2</sub> saturated electrolyte, their intensity is strongly diminished in the presence of CO<sub>2</sub>. This behavior has been previously observed for both Sn<sup>[43]</sup> and In<sup>[41,42]</sup> based catalysts and has been ascribed to the reaction of SnOx and InOx surfaces moieties with dissolved CO<sub>2</sub> to form a surface confined M-CO<sub>3</sub><sup>-</sup> intermediate (Scheme 1b). This intermediate is reduced during CO<sub>2</sub>RR catalytic turnover (i.e., at larger reductive bias) to yield formate and the metal site in its oxidized state, thus decreasing the magnitude of the MOx/M<sup>0</sup> redox peaks.

As already mentioned, “Sn<sub>1-x</sub>In<sub>x</sub>@In<sub>1-y</sub>Sn<sub>y</sub>O<sub>z</sub>” core@shell nanoparticles derived from in situ reduction of SnInOx provide a high CO<sub>2</sub>RR catalytic activity with a formate faradaic efficiency of 80% at an overall current density of  $-6.4 \pm 0.5 \text{ mA cm}^{-2}$  at  $-1.0 \text{ V}$  versus RHE, corresponding to a formate production rate of  $95.5 \mu\text{mol h}^{-1} \text{ cm}^{-2}$ . Considering the ultra-low mass of In and Sn present in the SnInOx films as determined by ICP-OES ( $m_{(\text{Sn}+\text{In})} = 12 \mu\text{g cm}^{-2}$ ,  $m_{\text{Sn}} = 8 \mu\text{g cm}^{-2}$ ,  $m_{\text{In}} = 4.3 \mu\text{g cm}^{-2}$ ), this performance corresponds to a remarkably high formate mass activity of  $437 \pm 15 \text{ A g}^{-1}_{(\text{Sn}+\text{In})}$  when referred to the total mass of Sn and In, as well as to a (theoretically) high mass activity of  $640 \pm 21 \text{ A g}_{\text{Sn}}^{-1}$  and  $1190 \pm 50 \text{ A g}_{\text{In}}^{-1}$  when referred to the mass of Sn and In separately, assuming each metal as the single CO<sub>2</sub>RR active component. With this mass activity, the SnInOx-films derived electrocatalysts presented in this work outperform the best reported Sn and closely match the best reported In based electrocatalysts reported in H-cell configuration so far. For comparison, the best Sn nanoparticulate system, that is, in situ reduced SnO<sub>2</sub> nanoparticles (diameter = 5 nm) supported on graphene,<sup>[40]</sup> was reported to have a mass activity of  $266 \text{ A g}_{\text{Sn}}^{-1}$  at  $-1.16 \text{ V}$  versus RHE, while the most active In based catalysts, that is, In nanoparticles (diameter = 6.1 nm) and In<sub>2</sub>O<sub>3</sub> nanoparticles (9.77 nm) supported on Vulcan were reported with  $215 \text{ A g}_{\text{In}}^{-1}$  and  $450 \text{ A g}_{\text{In}}^{-1}$  at  $-0.96 \text{ V}$  versus RHE respectively.<sup>[42]</sup> Further reports and comparisons of activity and selectivity of In and Sn-based electrocatalysts can be found in Table S1, Supporting Information.

### 2.1. In Situ SnInOx Film Reduction and Restructuring during CO<sub>2</sub>RR Electrolysis

As pointed out previously, the SnInOx films act as precatalysts and are reduced in situ during CO<sub>2</sub> electrolysis and strong

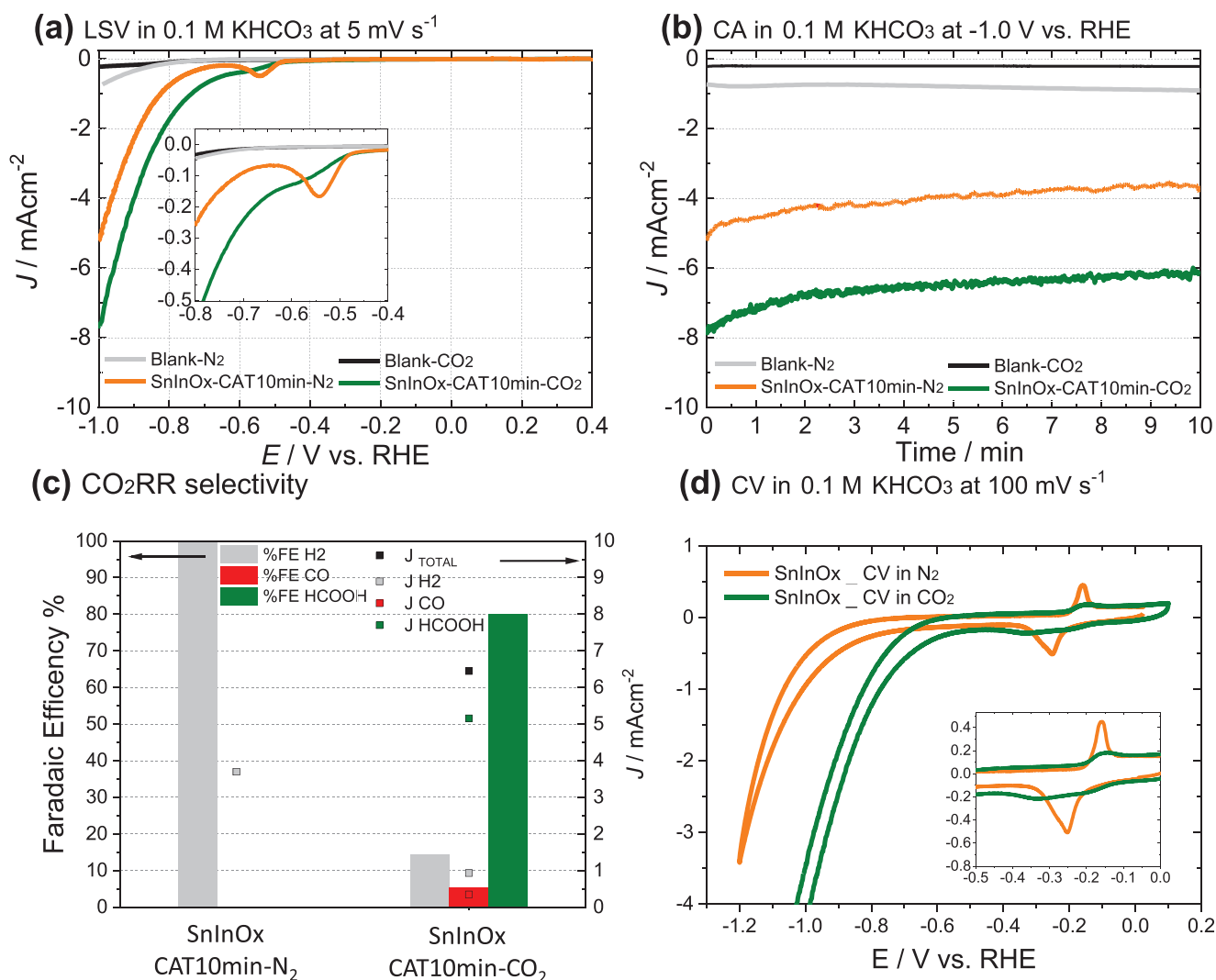


**Figure 1.** Electrochemical tests in aqueous 0.1 M  $\text{KHCO}_3$  performed with SnInOx planar films deposited on Glassy Carbon plate electrodes (GCE): a) cathodic linear sweep voltammetry (first sweep at  $5 \text{ mV s}^{-1}$ , inset displays an enlarged figure of the redox peak region associated to SnInOx reduction), followed by b) chronoamperometry at  $-1.0 \text{ V}$  versus RHE for SnInOx in  $\text{CO}_2$  saturated electrolyte (SnInOx- $\text{CO}_2$ , dark green) and SnInOx in  $\text{N}_2$  saturated electrolyte (SnInOx- $\text{N}_2$ , orange). Note: The blank measurements were done with pristine GCE plates. c) Faradaic efficiencies toward products such as formate (green bar), carbon monoxide (red bar) and  $\text{H}_2$  (grey bar) and respective current density (black dot). d) Stable cyclic voltammetry profile (typically after the fifth cycle) of SnInOx films cycled at  $100 \text{ mV s}^{-1}$  in  $\text{CO}_2$  (dark green) or  $\text{N}_2$  (orange) saturated 0.1 M  $\text{KHCO}_3$  and inset showing the potential region where SnInOx redox peaks occur.

structural changes occur. In order to investigate these changes, the SnInOx films were subjected to different  $\text{CO}_2$  electrolysis experiments and the resulting samples were denoted SnInOx-CAT@ $E-t$ , where  $E$  is the electrolysis potential (vs RHE) and  $t$  is the duration of the  $\text{CO}_2$  electrolysis test (i.e., the duration of the chronoamperometry step in the presence of  $\text{CO}_2$ ). The post electrolysis samples SnInOx-CAT@ $E-t$  were then characterized by ex situ by SEM, TEM, STEM, and GI-RXD (Note that unless otherwise specified, the ex situ characterization of samples is conducted on samples exposed to air after electrolysis tests).

After a typical  $\text{CO}_2$ RR electrolysis experiment at  $-1.0 \text{ V}$  versus RHE held for 10 min, denoted SnInOx-CAT@-1V\_10min, the originally planar and continuous SnInOx thin film (see SEM top view image, Figure 2b) is restructured into an array of nanoparticles with a size mode between 30 and 35 nm (SEM top

view image, Figure 2c). The overall metal composition of the SnInOx-CAT@-1V\_10min samples was assessed and EDX (performed in SEM top view mode, Figure S8, Supporting Information) and ICP-OES analysis revealed an overall In:Sn ratio of 0.6 (Table 1). Compared to the initial In:Sn ratio of 0.4 found for the starting SnInOx films, the composition of the reduced samples indicates a partial dissolution of Sn ( $\approx 1.5\text{--}2 \mu\text{g cm}^{-2}$ ) during the in situ reduction of planar SnInOx films to nanoparticles.

A detailed examination of the formed nanoparticles in a sample after 10 min of  $\text{CO}_2$  electrolysis at  $-1 \text{ V}$  versus RHE (i.e., in SnInOx-CAT@-1V\_10min) by transmission electron microscopy (TEM) (Figure 2d,f) revealed that each particle possesses a core@shell structure. From high-resolution transmission electron microscopy (HR-TEM) images (Figure 2d), a single crystalline core with a d-spacing of  $2.8 \text{ \AA}$  (Figure 2d) was identified;

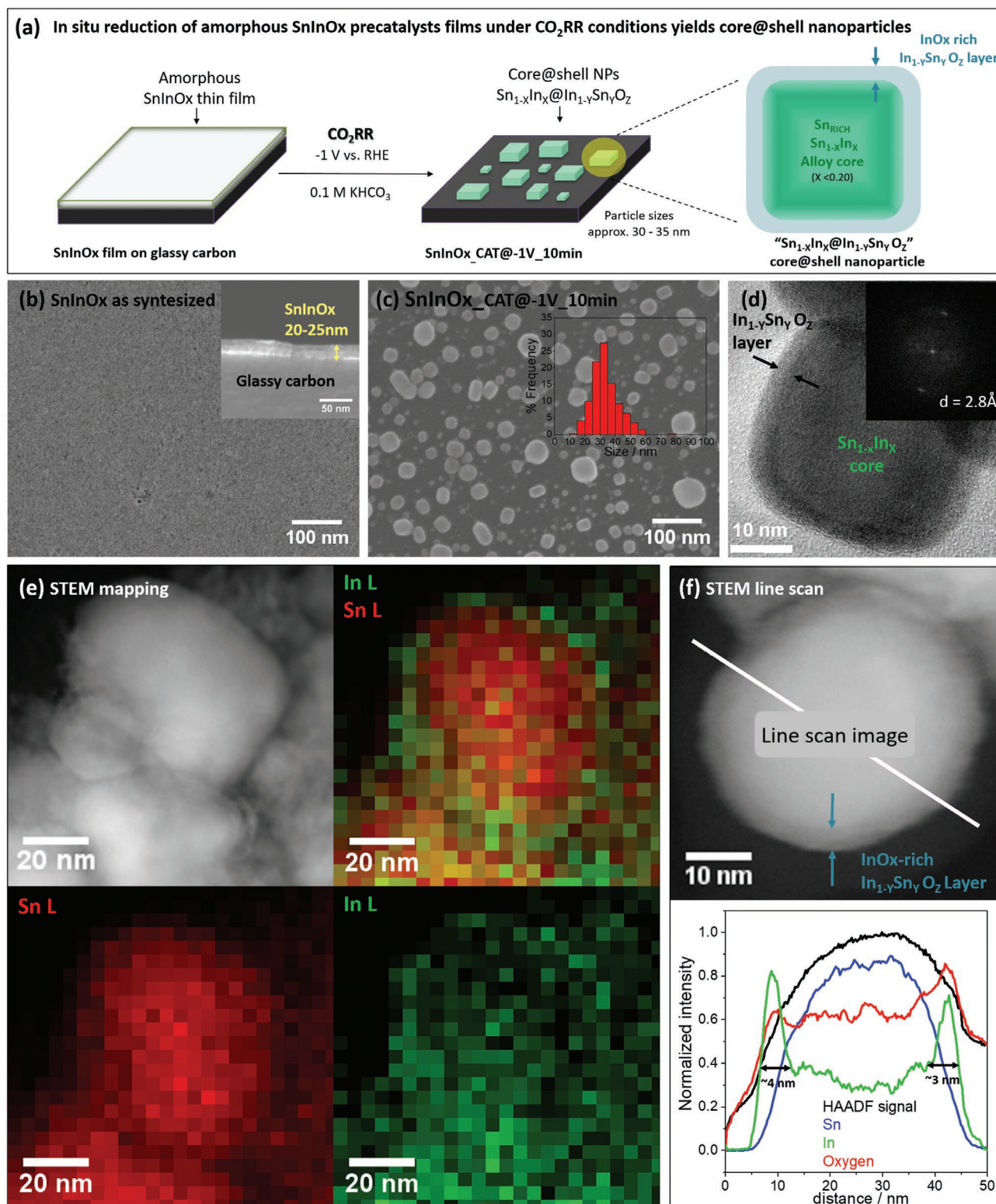


**Figure 2.** Structural analysis of SnInOx\_CAT@-1V\_10min films after 10 min of CO<sub>2</sub> electrolysis at -1.0 V in 0.1 M KHCO<sub>3</sub>; a) Schematic of the observed in situ transformation of SnInOx films into “Sn<sub>1-x</sub>In<sub>x</sub>@In<sub>1-y</sub>Sn<sub>y</sub>O<sub>z</sub>” core@shell nanoparticles. b) SEM image of an SnInOx planar film as-synthesized deposited on glassy carbon (the inset displays a SEM cross-section image showing the thickness of the SnInOx film). c) SEM image of an SnInOx film after 10 min of CO<sub>2</sub>RR electrolysis [SnInOx-CAT-10min]. d) TEM image of SnInOx\_CAT@-1V\_10min with corresponding FFT as inset. e) EDX STEM mapping of an “Sn<sub>1-x</sub>In<sub>x</sub>@In<sub>1-y</sub>Sn<sub>y</sub>O<sub>z</sub>” core@shell nanoparticle in SnInOx-CAT-10min [In-Sn mapping], f) STEM image and corresponding EDX line scan of a “Sn<sub>1-x</sub>In<sub>x</sub>@In<sub>1-y</sub>Sn<sub>y</sub>O<sub>z</sub>” core@shell nanoparticle in SnInOx\_CAT@-1V\_10min.

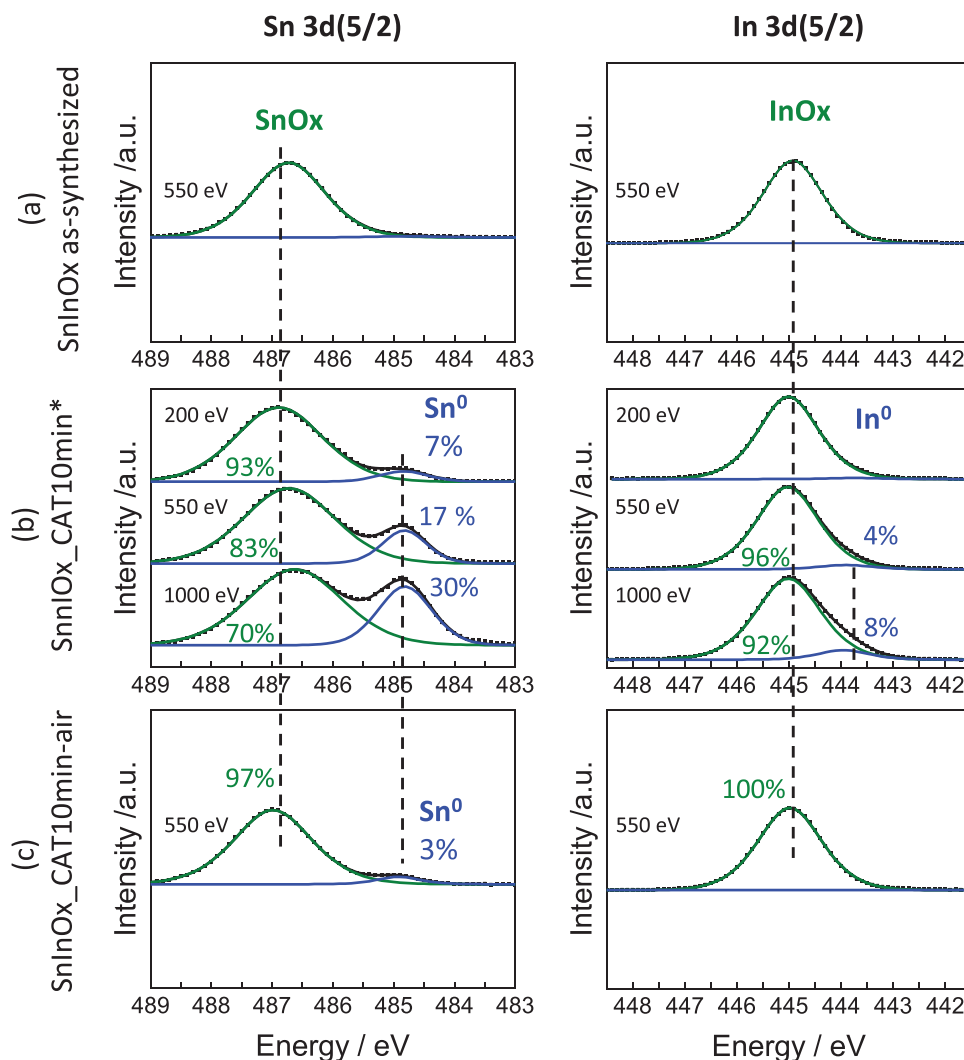


**Figure 3.** X-ray photoelectron spectroscopy (XPS) analysis of the surface composition of SnInO<sub>x</sub> derived composites. From left to right: XPS Sn 3d(5/2) and In 3d(5/2) core level spectra of a SnInO<sub>x</sub> film a) as synthesized, b) after CO<sub>2</sub>RR at  $-1.0$  V versus RHE (sample transfer under inert atmosphere to the XPS analysis chamber, SnInO<sub>x</sub>\_CAT10min\*) and c) after exposure of the sample to air for several hours (SnInO<sub>x</sub>\_CAT10min-air). The color code for the spectra and deconvolutions is experimental data (black dots), fit of the spectra (solid black line), metallic M<sup>0</sup> contribution (blue line) and MO<sub>x</sub> contribution (green line).

d-spacing, which is in good agreement with the major reflection at  $2\theta = 32^\circ$  ( $d = 2.79$  Å) observed in the grazing-incidence X-ray diffraction (GI-XRD) pattern of the SnInO<sub>x</sub>\_CAT@-1V\_10min sample (Figure S6, Supporting Information). The observed reflection can be ascribed either to tetragonal  $I41/amd$  Sn<sup>0</sup> ( $d(101) = 2.78$  Å) or to tin rich Sn<sub>1-x</sub>In<sub>x</sub> alloys such as tetragonal  $I41/amd$  In<sub>0.05</sub>Sn<sub>0.95</sub> ( $d(101) = 2.79$  Å) or hexagonal  $P6/mmm$  In<sub>0.2</sub>Sn<sub>0.8</sub> ( $d(100) = 2.79$  Å). However, the strong background signal from the glassy carbon electrode in GI-XRD and the ultra-thin nature of the nanoparticle array hinders the visibility of other reflections in the GI-XRD pattern limiting a definite assignment (Figures S6, Supporting Information). STEM EDX elemental mapping, as well as STEM EDX line scans (Figure 2e,f) revealed that the crystalline core of the formed nanoparticles is composed mostly of Sn (In:Sn ratio between 0.10–0.20), in line with the Tin-rich Sn<sub>1-x</sub>In<sub>x</sub> (with  $x < 0.20$ ) alloy phases mentioned in the GI-XRD section before. As seen in

Figure 2d,f, this crystalline Tin-rich core is surrounded by an amorphous indium tin oxide shell enriched with Indium (layer thickness  $\approx 3$  nm).

The surface composition of the SnInO<sub>x</sub> films as synthesized and after CO<sub>2</sub>RR electrolysis was further investigated by X-ray photoelectron spectroscopy (XPS). The spectra of the Sn 3d (5/2) and In 3d (5/2) core levels collected at a photoelectron kinetic energy of 550 eV are shown in Figure 3. At this kinetic energy, the inelastic mean free path in the composite is roughly 1.2 nm,<sup>[62]</sup> indicating that the composition information gained by XPS corresponds to the outer amorphous shell of the in situ formed nanoparticles (see TEM Figure 2e). Both Sn3d and In3d core levels appear as doublet, but only the 5/2 component is depicted.

In the as-synthesized SnInO<sub>x</sub> film, the Sn3d (5/2) and In3d (5/2) core levels exhibit one symmetric peak respectively located at 486.7 and 444.9 eV (Figure 3a), assigned to Sn<sup>4+</sup> and

In<sup>3+</sup> respectively. The O1s core level, displayed in Figure S7, Supporting Information, exhibits three main contributions at 530.5, 532.1, and 533.4 eV ascribed to SnInOx lattice O (M–O), surface hydroxide (M–OH), and adsorbed water, respectively. The results are in agreement with previously reported values for SnO<sub>2</sub>,<sup>[38,40]</sup> In<sub>2</sub>O<sub>3</sub>,<sup>[41,42]</sup> and ITO.<sup>[63]</sup> The XPS quantitative analysis (see Table 1) indicates that the as-synthesized SnInOx films have an In:Sn surface ratio of 0.3, which is in good agreement with the In:Sn bulk ratio of 0.4 found by EDX and ICP analysis (Table 1).

After CO<sub>2</sub>RR electrolysis the sample SnInOx\_CAT@-1V\_10min was removed from the electrolyte under bias (–1 V), handled and stored under inert atmosphere prior and during transfer to the XPS analysis chamber (See experimental details). This sample was denoted “SnInOx\_CAT10min\*” (see Figure 3b). All samples investigated in XPS after CO<sub>2</sub>RR were handled this way. Quantitative analysis of the XPS data revealed a total In:Sn surface ratio of 1.3, that is, more than twice the bulk In:Sn ratio of ≈0.6 found by EDX and ICP-OES for this sample, providing further evidence for the segregation of In to the surface of the particles to form “Sn<sub>1-x</sub>In<sub>x</sub>@In<sub>1-y</sub>Sn<sub>y</sub>O<sub>z</sub>” core@shell nanoparticles. An O/M<sub>In+Sn</sub> ratio of ≈1.1 was found, yielding an approximate shell composition denoted by the formula In<sub>1-y</sub>Sn<sub>y</sub>O<sub>z</sub> with Y ≈ 0.4 and Z ≈ 1. The O 1s XPS spectra of the SnInOx\_CAT@-1V\_10min sample revealed the presence of lattice oxygen (M–O) and surface hydroxide (M–OH) moieties at the surface of the particles. Precise deconvolution of the O 1s signal was however hindered by the presence of KHCO<sub>3</sub> electrolyte residues (Figure S7, Supporting Information).

Despite the reductive conditions, both oxidized Sn and In species were revealed to dominate the surface composition of the in situ formed particles (as seen in the Sn 3d (5/2) and In 3d (5/2) XPS spectra in Figure 3b). The deconvolution of the In 3d (5/2) XPS peak reveals that In is present predominantly as In<sup>3+</sup> (96 at%), as evidenced by the large peak at 444.9 eV (Figure 3b), probably in the form of amorphous In<sub>2</sub>O<sub>3</sub> or In(OH)<sub>3</sub>, denoted as “InOx,” as indicated by the presence of lattice O and –OH contributions observed in the O1s core level (Figure S7, Supporting Information). Minor amounts of metallic In<sup>0</sup> (4 at%) are also observed, as evidenced by the peak at 443.9 eV.

Sn surface speciation reveals a predominant Sn<sup>4+</sup> contribution (86 at%), as evidenced by the peak at 486.7 eV, corresponding most likely to Sn<sup>4+</sup> in SnO<sub>2</sub> or SnO(OH)<sub>2</sub>, while the metallic Sn<sup>0</sup> component (484.9 eV) was found to account for 17 at%. The high symmetry of the peak at 486.7 eV strongly indicates the absence of Sn<sup>2+</sup>. However, the presence of Sn<sup>2+</sup> at the surface of the particles cannot be totally ruled out. In the following the peak corresponding to oxide Sn species is denoted as “SnOx.”

To gain further insight about the segregation into “Sn<sub>1-x</sub>In<sub>x</sub>@In<sub>1-y</sub>Sn<sub>y</sub>O<sub>z</sub>” core@shell nanoparticles, the Sn 3d and In 3d core levels were investigated at increasing probing depth with increasing photoelectron kinetic energy ranging from 200, 550, to 1000 eV, corresponding roughly to an inelastic mean free path of 0.6, 1.2, and 1.8 nm, respectively (Figure 3b).<sup>[62]</sup> The results indicate that the contribution of metallic/reduced Sn<sup>0</sup> (484.9 eV) and In<sup>0</sup> (443.9 eV) increases with increasing probing depth, while the In/Sn ratio decreases (Table 1). These results, in line with the STEM EDX line scan measurements discussed

earlier (vide supra), provide further evidence for the formation of “Sn<sub>1-x</sub>In<sub>x</sub>@In<sub>1-y</sub>Sn<sub>y</sub>O<sub>z</sub>” core@shell nanoparticles, composed of an alloyed Sn<sup>0</sup>-rich Sn<sub>1-x</sub>In<sub>x</sub> core surrounded by an InOx-rich In<sub>1-y</sub>Sn<sub>y</sub>O<sub>z</sub> shell, during CO<sub>2</sub> electrolysis.

A sample after CO<sub>2</sub>RR electrolysis, that is, SnInOx\_CAT@-1V\_10min, was also analyzed by XPS after exposure to air for a couple of hours, denoted “SnInOx\_CAT10min-air” in Figure 3c. As seen by comparing Figure 3b and c, the contribution of metallic/reduced Sn<sup>0</sup> (484.9 eV) and In<sup>0</sup> (443.9 eV) were found to decrease upon air exposure. While in the sample transferred under inert atmosphere (energy 550 eV with a penetration depth of ≈1.2 nm) the metallic contribution was as high as 17% and 4% for Sn<sup>0</sup> and In<sup>0</sup>, respectively, only little (≈3%) or no metallic contribution was found for Sn and In, respectively, in the sample exposed to air. While these results indicate that the catalyst surface is susceptible to reoxidation once the bias is removed and the sample is exposed to air, they also prove the efficacy of transferring the post electrolysis sample under inert atmosphere to the XPS analysis chamber for preventing oxidation in air. To conclude, this procedure allowed us to investigate the surface composition of the reduced core@shell nanoparticles with minimized impact of oxidation by air. Accordingly, the observation of a surface mainly composed of SnOx and InOx in the sample transferred under inert atmosphere (SnInOx\_CAT10min\*) strongly points to the presence of persistent oxidized species on the catalyst's surface during CO<sub>2</sub>RR, as has been previously proposed for Sn<sup>[43,52]</sup> and In<sup>[41]</sup> surfaces based on in situ ATR-IR, Raman and XAS observations. These results also indicate that the amorphous In<sub>1-y</sub>Sn<sub>y</sub>O<sub>z</sub> shell measured in ex situ TEM analysis is most likely present (at least partially) under CO<sub>2</sub> electroreduction conditions.

Interestingly, the sample exposed to air after a first CO<sub>2</sub> electrolysis experiment of 10 min, denoted SnInOx\_CAT\_10min-air, displays increased formate faradaic efficiency of 90% in a second electrolysis run, at however significantly lower current density, and hence formate production rates, in comparison to the unexposed samples (Figure S3, Table S2, Supporting Information). These results are in good agreement with reports indicating improved formate selectivity in oxide enriched Sn<sup>[38–40,43]</sup> and In<sup>[41,42]</sup> based CO<sub>2</sub>RR electrocatalysts.

As has been discussed so far, SnInOx thin films undergo drastic structural changes during electrocatalytic CO<sub>2</sub> reduction to form “Sn<sub>1-x</sub>In<sub>x</sub>@In<sub>1-y</sub>Sn<sub>y</sub>O<sub>z</sub>” core@shell nanoparticles. In this context, different reductive pretreatments were essayed to induce this transformation by purpose with the attempt to reach a structurally steady and active state of the catalyst. The effect of diverse electrochemical reducing treatments on the catalyst structure and activity was thereby investigated, namely the pre-reduction of SnInOx planar films by extensive potential cycling in the reductive range (–0.4 to –1.2 V vs RHE) in either N<sub>2</sub>-saturated electrolyte or CO<sub>2</sub> saturated electrolyte (see details in Figure S3, Supporting Information). For all samples investigated a reduction/restructuring of the SnInOx films into an array of “Sn<sub>1-x</sub>In<sub>x</sub>@In<sub>1-y</sub>Sn<sub>y</sub>O<sub>z</sub>” core@shell nanoparticles with an In:Sn bulk ratio close to 0.6 and an In rich oxide layer (<5 nm) occurs (Figure S4, Supporting Information). These results indicate that such “Sn<sub>1-x</sub>In<sub>x</sub>@In<sub>1-y</sub>Sn<sub>y</sub>O<sub>z</sub>” core@shell structures seem to be favored under various reducing conditions. Similar In surface segregation in form of In(OH)<sub>3</sub> has



been previously observed under CO<sub>2</sub>RR at  $-0.6\text{V}$  versus RHE for bimetallic Cu–In catalysts.<sup>[57]</sup> Despite the structural similarities among all SnInOx derivatives, all pretreatments essayed resulted in overall less catalytically active materials (Figure S3, Table S2, Supporting Information). The SnInOx samples pre-reduced in N<sub>2</sub> or CO<sub>2</sub> saturated electrolyte, were found to yield lower overall catalytic current densities ( $-4.1\text{ mA cm}^{-2}$  and  $-4.6\text{ mA cm}^{-2}$  at  $-1.0\text{ V}$  respectively) in CO<sub>2</sub> saturated electrolyte than the in situ reduced InSnOx planar films ( $-6.4\text{ mA cm}^{-2}$ ); a result, which might relate to the formation of larger nanoparticles (favored nanoparticle sizes > 30 nm, Figure S4, Supporting Information) leading to an overall lower electroactive surface area (Table S2, Supporting Information). Furthermore, SnInOx samples pre-reduced in N<sub>2</sub>- or CO<sub>2</sub>-saturated electrolyte were found to exhibit decreased formate faradaic efficiency of 76% and 63%, respectively. The analysis of the shell composition of the pre-reduced samples conducted by XPS analysis in samples handled, stored, and transferred under inert atmosphere (see details in Figure S7, Supporting Information) revealed that the SnInOx films pre-reduced in CO<sub>2</sub> saturated electrolyte, which provide the lowest formate selectivity (63%), display the highest metallic Sn<sup>0</sup> contribution (30%); results, which are in line with recent literature reports, demonstrating higher hydrogen evolution activity for metallic states, while higher formate production activity was associated with oxide enriched Sn<sup>[38–40,43]</sup> and In<sup>[41,42]</sup> based CO<sub>2</sub>RR electrocatalysts. To summarize, the results obtained for the pre-reduction treatments indicate that in situ reduction/restructuring of untreated SnInOx films during CO<sub>2</sub>RR provides optimal catalytic performance with high current density and high selectivity for formate production ( $\text{FE}_{\text{formate}} = 80\%$ ), due to the combination of formation of small particles and MOx-enriched surface compositions.

Despite our efforts to handle the samples under inert atmosphere to avoid surface oxidation by air exposure, one has to note, that our ex-situ TEM investigation of the core@shell particles could not entirely be realized without exposing the samples to air (even if just for a few minutes, that is, the time necessary to place the sample in the TEM holder and to insert it in the transfer lock). Hence our ex situ TEM investigation does not allow to determine unambiguously whether the few nm oxide layer (Figure 2d; Figure S4, Supporting Information) is present under catalytic CO<sub>2</sub>RR conditions in spite of the applied reductive bias, or if the oxidic shell is spontaneously oxidized/formed after the electrocatalytic experiment upon removal of the reductive bias and exposure to air. To gain further insight in this matter, we compared samples handled under inert atmosphere and analyzed directly after CO<sub>2</sub> electroreduction with a minimal air exposure of approximately 2 min (SnInOx\_CAT@-1V\_10min) with samples intentionally exposed to air for several days. The comparison revealed the presence of an oxide shell with similar thickness ( $\approx 3\text{ nm}$ ) for all samples investigated, independently of their contact time with air (Figure S5, Supporting Information). As no difference in shell thickness was observed for different exposure time, these results indicate to us that the observed oxidic layer is likely to be present during CO<sub>2</sub>RR and is not simply the product of oxidation of the nanoparticles upon air exposure. Further clarification in that matter was provided by our XPS study (vide supra), which

was performed on samples handled, stored, and transferred under inert atmosphere without any air exposure. For example, the XPS analysis of the sample SnInOx\_CAT@-1V\_10min\* (Figure 3b), handled, stored, and transferred under inert atmosphere, indicates that the surface of the core@shell nanoparticles is, besides a small portion of metallic Sn, predominantly composed of SnOx and InOx; result, which strongly suggests to the persistence of an oxidic surface layer on the surface of the core@shell nanoparticles under CO<sub>2</sub> reduction conditions. Our results are also in line with recent in situ spectroscopic investigations on tin oxide<sup>[43,52]</sup> and indium oxide<sup>[41]</sup> derived catalysts under CO<sub>2</sub> electroreduction conditions.

## 2.2. Long Term CO<sub>2</sub>RR Electrolysis

Among the pretreatments assayed, it was found that untreated SnInOx films offer the best compromise with a high faradaic efficiency (80%) and high mass activity ( $437\text{ A g}_{\text{In+Sn}}^{-1}$ ) for formate. The long-term performance of untreated SnInOx films for CO<sub>2</sub>RR electrolysis was evaluated in a custom-made two-compartment cell, separated by a Nafion 117 membrane and provided with a constant inlet of CO<sub>2</sub> at  $30\text{ mL min}^{-1}$  in CO<sub>2</sub> saturated  $0.1\text{ M KHCO}_3$  (pH 6.8) (see details in Figure S2b, Supporting Information). The CO<sub>2</sub> electroreduction test was conducted for 10 h at  $-1.0\text{ V}$  versus RHE and the resulting sample is named SnInOx\_CAT@-1V\_10h. The CO<sub>2</sub>RR catalytic current density and the different reaction products (H<sub>2</sub>, CO and formate) obtained over time are presented in Figure 4a. Remarkably, a sustained formate faradaic efficiency around 80% is observed for 4 h and this only slightly drops to 70% after 10 h of operation. Regarding the minor products, H<sub>2</sub> and CO, the H<sub>2</sub> faradaic efficiency decreases from 15% to 11%, while the CO faradaic efficiency grows from 4.5% to 9% within 10 h of extended electrolysis. No additional products were detected in the liquid phase by <sup>1</sup>H-NMR or HPLC.

The overall catalytic current density profile of SnInOx\_CAT@-1V\_10h exhibits an interesting behavior over time: while the current density initially drops from  $-7\text{ mA cm}^{-2}$  to  $-6.2\text{ mA cm}^{-2}$  within the initial 10–20 min of electrolysis, a sustained growth in current density reaching  $-8.3\text{ mA cm}^{-2}$  after 10 h of electrolysis is observed (Figure 4a). The pre-reduced SnInOx samples exhibited a similar behavior with initial lower current densities showing a less steep but sustained growth in current density throughout the 10 h of electrolysis; the results are shown in Figure S10, Supporting Information. The progressive growth of the catalytic current density is most likely caused by an increase of electrochemical surface area over time induced by a decrease in particle size (Figure 4b). After an extended electrolysis for 10 h at  $-1.0\text{ V}$  versus RHE, the formed particles were found to have a bimodal size distribution with a predominant contribution of small particles (with sizes < 30 nm) centered at  $\approx 20\text{ nm}$  and a smaller contribution of large particles (with sizes > 30 nm) centered at  $\approx 50\text{ nm}$ . The predominance of small particles with diameters < 30 nm was significantly higher in this sample, that is, for prolonged electrolysis time (10 h at  $-1\text{ V}$  versus RHE, SnInOx\_CAT@-1V\_10h, Figure 4b) than for short

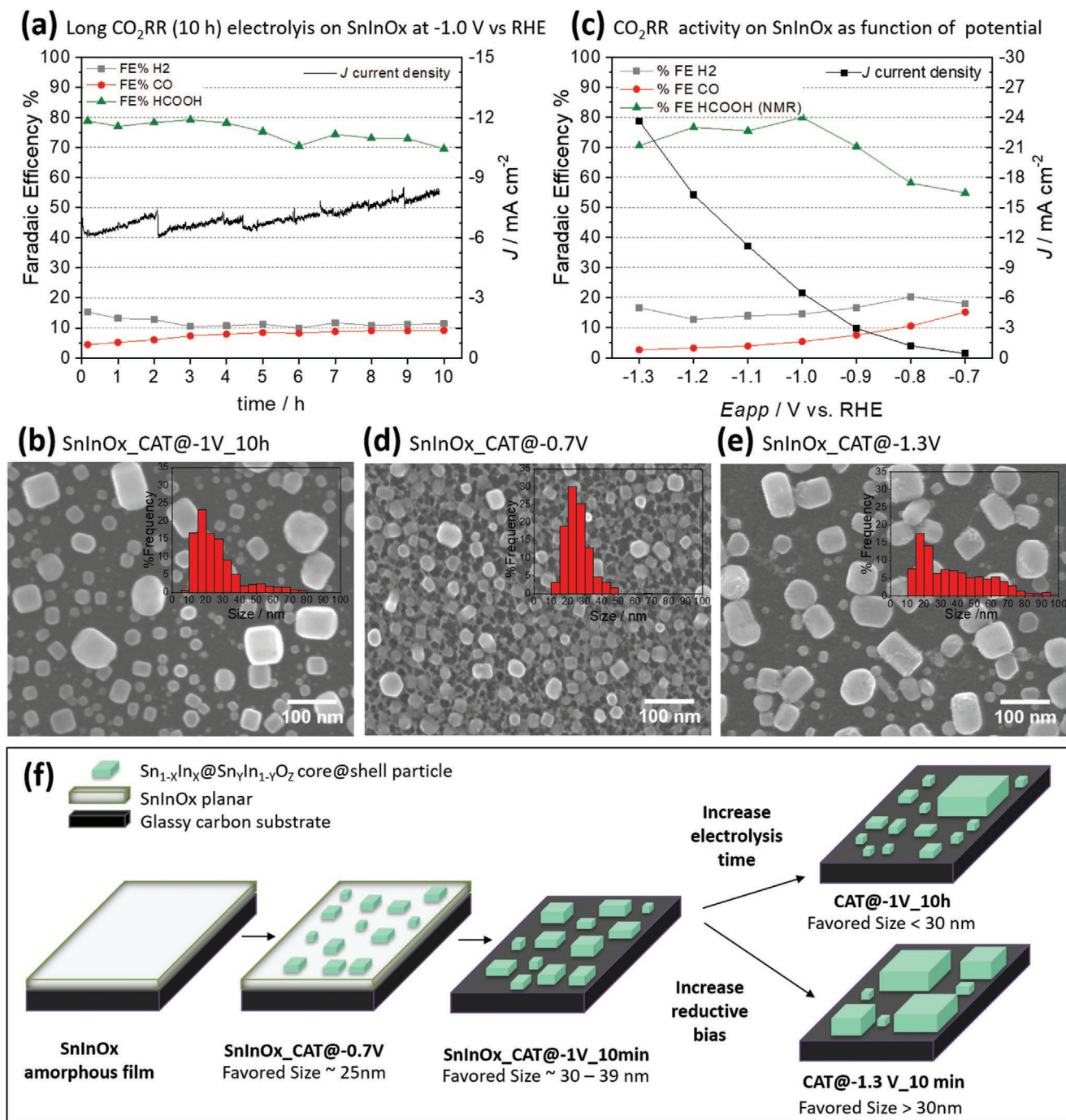


**Figure 4.** Effect of CO<sub>2</sub>RR electrolysis time and applied potential on the catalytic behavior of untreated SnInOx electrodes. a) CO<sub>2</sub>RR catalytic activity during electrolysis of untreated SnInOx at -1.0 V for 10 h (SnInOx\_CAT@-1V\_10h), and b) associated SEM image and particle size distribution. c) CO<sub>2</sub>RR catalytic activity of untreated SnInOx at different cathodic potentials between -0.7 and -1.3 V, d) associated SEM images of SnInOx after electrolysis at -0.7 V for 1 h (SnInOx\_CAT@-0.7V), and e) after electrolysis at -1.3 V for 10 min (SnInOx\_CAT@-1.3V). f) Scheme of Sn<sub>1-x</sub>In<sub>x</sub>@Sn<sub>1-y</sub>In<sub>1-y</sub>O<sub>z</sub> core@shell particle size dynamics during CO<sub>2</sub>RR.

electrolysis time (10 min at -1V versus RHE, SnInOx\_CAT@-1V\_10min, Figure 2c). In consequence, as electrolysis time increases, small particles (<30 nm) start to dominate the size distribution. These results indicate a dynamic nature of the particles structure and size during prolonged electrolysis. It appears that the formation of larger particles is overruled by

the concomitant formation of small particles. A similar particle dynamic resulting in a bimodal particle size distribution dominated by small particles (<30 nm) was also observed for pre-reduced SnInOx films after prolonged electrolysis experiments (10 h). Further details can be found in Figure S11, Supporting Information.

### 2.3. Effect of Electrolysis Potential on CO<sub>2</sub>RR Catalytic Activity

The performance of SnInOx for CO<sub>2</sub>RR was evaluated at different applied potentials ranging from  $-0.7$  V to  $-1.3$  V versus RHE (see experimental details). The catalytic current density, H<sub>2</sub>, CO, and formate faradaic efficiency were examined at each essayed potential (Figure 4c). No additional CO<sub>2</sub> conversion products were detected in the evaluated potential range. The untreated SnInOx sample exhibits a high formate faradaic efficiency over all the evaluated potential range, increasing from 55% to 80% between  $-0.7$  V and  $-1.0$  V, followed by a slight decrease from 80% down to 70% between  $-1.0$  and  $-1.3$  V. In contrast, the H<sub>2</sub> faradaic efficiency decreases from 20% to 13% between  $-0.7$  V and  $-1.2$  V followed by a small increase up to 16.6% between  $-1.2$  V and  $-1.3$  V versus RHE. The CO faradaic efficiency, in turn, was found to steadily decrease from 15% to 2.6% with increasing reductive potential between  $-0.7$  V and  $-1.3$  V. Note that in the lower bias range ( $-0.7$  to  $-0.8$  V) added FE of different products yield a total of  $\approx 90\%$ . The reminder of the charge is likely to correspond to the in situ reduction of the mixed SnInOx oxide. The effect of electrolysis potential on the CO<sub>2</sub>RR activity of the pre-reduced SnInOx derivatives was also examined (Figure S10, Supporting Information). At low reductive potentials ( $-0.7$  V vs RHE), the SnInOx films pre-reduced by cyclic voltammetry in CO<sub>2</sub> or N<sub>2</sub> sat. electrolyte, both favor H<sub>2</sub> production with faradaic efficiencies of 40% and 62%, respectively, and display lower formate faradaic efficiencies (35% and 22%, respectively) than untreated SnInOx at the same potential (SnInOx\_CAT@-0.7V, FE formate 55%). This result demonstrates once more that only the in situ transformation of untreated SnInOx film during CO<sub>2</sub> electrolysis leads to a catalyst that favors CO<sub>2</sub> reduction rather than hydrogen evolution. Further details on potential dependent activity on pre-reduced SnInOx derivatives is displayed in supporting information in Figure S10, Supporting Information.

### 2.4. Particle Size Dynamics

Regarding the particle size distribution, an interesting effect of the electrolysis potential on the particle size dynamics was found. The SEM images and particle size distributions for untreated SnInOx films investigated after catalytic tests at different electrolysis potentials, SnInOx-CAT@E with  $E = -0.7$  V and  $-1.3$  V versus RHE, reveal that the in situ particle formation is a dynamic process of particle ripening and growth with a strong dependence on applied electrolysis potential (Figure 4d,e). After electrolysis for 1 h at  $-0.7$  V versus RHE (SnInOx\_CAT@-0.7V) the restructuring of the SnInOx material is at an early stage of particle growth and in situ formed particles with a mode size of 25 nm are found embedded within/surrounded by a remaining amorphous SnInOx film matrix, as can be seen in Figure 4d. A schematic depiction of this process is shown in Figure 4f. Expectedly, the capacitance of the film at this stage ( $75 \mu\text{F cm}^{-2}$ , see Figure S9 and Table S4, Supporting Information) is very similar (if any slightly smaller) to that of the original SnInOx film ( $80 \mu\text{F cm}^{-2}$ ). In comparison, the film after 10 min of electrolysis at  $-1.0$  V versus RHE, that is, SnInOx\_CAT@-1V\_10min (Figure 2c; Figure S11, Supporting

Information), evidences further particle formation and growth (with particles of similar shape but larger mode size of 34 nm) as well as disappearance of any amorphous residues of the original SnInOx film. Accordingly, a significantly larger capacitance of  $313 \mu\text{F cm}^{-2}$  is found (Table S4, Supporting Information). Furthermore, the film submitted to high cathodic bias of  $-1.3$  V versus RHE for 10 min, SnInOx-CAT@-1.3 V, exhibits a very broad particle size distribution tailing toward larger particle sizes in the range 30–100 nm (Figure 4e), indicating that increasing cathodic bias induces particle growth. Accordingly, at this high reductive potential a low capacitance of  $114 \mu\text{F cm}^{-2}$  is found. Similarly, pre-reduced films submitted to electrolysis experiments conducted at large reductive bias, SnInOx\_pre-reduced-N<sub>2</sub>\_CAT@-1.3V and SnInOx\_pre-reduced-CO<sub>2</sub>\_CAT@-1.3V, yield particles with a broad size distribution dominated by particles larger than 30 nm, as can be seen in Figure S11i–k, Supporting Information.

Overall, all SnInOx derivatives, in situ reduced or pre-reduced, exhibit the same particle size dynamics during CO<sub>2</sub>RR electrolysis: long electrolysis time (10 h) at  $-1.0$  V versus RHE favors the formation of small particles with sizes  $< 30$  nm, while high applied reductive bias ( $-1.3$  V vs RHE for 10 min) leads to the formation of large particles  $> 30$  nm (Figure S11, Supporting Information). A schematic summary of the observed particle growth dynamics is shown in Figure 4f. Structural investigations by HR-TEM and GI-XRD (Figure S12, Supporting Information) revealed that, in spite of the particle size dynamics leading to variable particle sizes, all samples investigated after electrolysis tests for different times or potentials are composed of core@shell nanoparticles (with a metallic tin-rich Sn<sub>1-x</sub>In<sub>x</sub> core and an oxidic indium-rich In<sub>1-y</sub>Sn<sub>y</sub>O<sub>z</sub> shell (Sn<sub>1-x</sub>In<sub>x</sub>@In<sub>1-y</sub>Sn<sub>y</sub>O<sub>z</sub>), as was further confirmed by STEM line scan analysis (Figure S13, Supporting Information).

One has to note, that the used reductive pretreatments, either in CO<sub>2</sub> saturated electrolyte or in N<sub>2</sub> saturated electrolyte, are not sufficient to bring the SnInOx-derived catalysts to a steady state in terms of particle growth. Indeed, after reductive pretreatment, further particle size changes are observed for both types of pre-reduced SnInOx films after extended (10 h) or high potential ( $-1.3$  V) electrolysis experiments (Figures S11,S12, Supporting Information). Similar roughening and morphological surface changes have been observed during CO<sub>2</sub>RR for other Sn<sup>[38,43]</sup> and In<sup>[41]</sup> based electrocatalysts. However, no previous study had investigated the surface changes in detail. In the case of Cu surfaces, a detailed Electrochemical Scanning Tunneling Microscopy (ECSTM) investigation revealed that single crystals exhibit surface re-structuration during CO<sub>2</sub>RR,<sup>[64,65]</sup> indicating that surface changes and evolution during electroreduction of CO<sub>2</sub>, might be an important aspect of CO<sub>2</sub>RR electrocatalysis that must be further investigated.

## 3. Conclusion

The evaluation of the CO<sub>2</sub>RR activity of amorphous and planar SnInOx films deposited on glassy carbon revealed that these films are highly active for CO<sub>2</sub> reduction toward formate. More than just a catalyst, these films turned out to be ideal precatalysts for the in situ formation under CO<sub>2</sub>RR conditions of

“Sn<sub>1-x</sub>In<sub>x</sub>@In<sub>1-y</sub>Sn<sub>y</sub>O<sub>z</sub>” core@shell nanoparticles, composed of an Sn-rich core (of the type In<sub>0.2</sub>Sn<sub>0.8</sub>) and an In-rich amorphous oxidic shell, with a mode size of 33 nm. These in situ formed “Sn<sub>1-x</sub>In<sub>x</sub>@In<sub>1-y</sub>Sn<sub>y</sub>O<sub>z</sub>” core@shell nanoparticles provide a high faradaic efficiency (80%) and a high mass activity (437 A g<sub>In+Sn</sub><sup>-1</sup>) for formate, and, to the best of our knowledge, outperform, despite their larger size and hence lower active surface area, the best reported mass activities for Sn-Oxide and In-Oxide based systems so far (266 A g<sub>Sn</sub><sup>-1</sup> for SnO<sub>2</sub> nanoparticles (5nm) supported on graphene<sup>[40]</sup> and 300 A g<sub>In</sub><sup>-1</sup> for (6.1 nm) nanoparticles supported on Vulcan<sup>[42]</sup>).

The indium segregation toward the surface of these particles is perhaps the most interesting feature of the SnInOx-derived catalysts for the CO<sub>2</sub>RR. Indium and especially oxidized indium is suspected to favor high formate faradaic efficiency (80%) for the following reasons: 1) In-based catalysts have been reported to provide higher formate faradic efficiencies than Sn-based catalysts.<sup>[7,9,13,16,17,40–43]</sup> 2) XPS analysis indicates that >95% of the In content at the surface is found as InOx species and MOx surface species are known to favor formate selectivity.<sup>[38–43]</sup> 3) The positive influence of InOx surface species on the formate selectivity from 80% to 93% has also been observed in the present work for SnInOx derived catalysts upon air exposure. As such, the in situ formed “Sn<sub>1-x</sub>In<sub>x</sub>@In<sub>1-y</sub>Sn<sub>y</sub>O<sub>z</sub>” core@shell offer advantageous cooperation between the conductive alloy core and the InOx enriched shell that favors formate selectivity.

In addition, structural investigations of the in situ formed “Sn<sub>1-x</sub>In<sub>x</sub>@In<sub>1-y</sub>Sn<sub>y</sub>O<sub>z</sub>” core@shell particles during CO<sub>2</sub>RR electrolysis revealed a rather dynamic nature of the catalyst structure and morphology. Continuous changes in particle size distribution were observed along extended electrolysis. Long electrolysis (10 h) experiments at –1.0 V versus RHE favor the formation of small particles with sizes < 30 nm with a comparatively high surface area for CO<sub>2</sub> conversion, inducing a current density growth over the time course of electrolysis and a selectivity decay from 80% to 70% in the experiment time scale. Electrolysis experiments at higher reductive bias up to –1.3 V versus RHE favor the growth of larger particles with sizes > 30 nm and smaller active surface areas. Interestingly, extensive ex situ SEM, TEM, STEM, and EDX analysis corroborates that the “Sn<sub>1-x</sub>In<sub>x</sub>@In<sub>1-y</sub>Sn<sub>y</sub>O<sub>z</sub>” core@shell structure is present in all investigated samples despite the particle size changes.

All in all, our results indicate that amorphous tin-rich ITO is a suitable pre-catalyst to form highly active and highly selective core@shell nanoelectrocatalysts for CO<sub>2</sub> reduction to formate. In addition, our results indicate that especially amorphous oxides are interesting pre-catalysts for the design of metal oxide derived electrocatalysts for CO<sub>2</sub>RR and that in particular bimetallic amorphous oxides can give rise to interesting bimetallic metal@metal oxide core@shell structures under CO<sub>2</sub> reduction conditions allowing to explore synergies between different metals and metal oxides.

## 4. Experimental Section

**SnInOx Thin Film Synthesis:** Prior to SnInOx film deposition, the glassy carbon electrodes were extensively cleaned in aqua regia (HNO<sub>3</sub>:HCl 1:3) at 90 °C, washed with Millipore water (18.2 mΩ) at 90 °C to remove acid residues and finally washed exhaustively with Millipore water (18.2 mΩ).

The electrodes were then polished with alumina suspensions with 1 μm and 0.05 μm particle size (Buehler), subsequently cleaned by ultrasonic treatment in water, isopropanol, and acetone, and dried overnight at 100 °C prior to insertion into the glovebox for SnInOx film deposition.

SnInOx films were prepared by thermal decomposition of an organometallic single-source precursor Indium(III)-tin(II)-tri-tert-butyl-oxide (InSn(OtBu)<sub>3</sub> (in short ITBO)).<sup>[53,54,56]</sup> Due to the O<sub>2</sub>/water sensitive nature of ITBO, it must be handled inside an inert and dry glove box. The ITBO precursor was dissolved in dry toluene (200 mg mL<sup>-1</sup>) and spin-coated onto a double side polished glassy carbon plate (SIGRADUR G from HTW GmbH) over an area of 1.5 cm<sup>2</sup>. After drying, the obtained film was calcined 1) in air at 400 °C for 2 h and 2) under 5% H<sub>2</sub> in N<sub>2</sub> atmosphere at 300 °C for 90 min. An amorphous SnInOx oxide thin film was obtained with a thickness of approximately 20–25 nm, as determined by SEM (Figure S1, Supporting Information), and a combined metal loading (Sn + In) of 12 μg cm<sup>-2</sup>, as determined by ICP-OES.

**Electrochemical Measurements:** SnInOx films coated onto glassy carbon plates were used as working electrode, an Ag/AgCl (DriRef2 from WPI) as a reference electrode, and a platinum mesh as counter electrode. To control the potential of the working electrode a Potentiostat SP-200 from Biologic was used. The electrolyte, unless otherwise specified, was aqueous 0.1 M KHCO<sub>3</sub>, prepared from reagent grade KHCO<sub>3</sub> (99.97% purity, Sigma-Aldrich) and Millipore water (18.2 mΩ). All electrochemical data presented (cyclic voltammetry (CV), linear sweep voltammetry (LSV), and chronoamperometry (CA)) were automatically corrected for 85% iR drop by the potentiostat.

**Cyclic Voltammetry Experiments:** Cyclic voltammetry experiments were performed in a typical three electrode cell and N<sub>2</sub> or CO<sub>2</sub> were purged through the electrolyte for 15–20 min prior the measurement.

**Bulk Electrolysis Experiments:** Bulk electrolysis experiments were carried out in two different electrochemical cells. Short CO<sub>2</sub>RR activity tests at different potentials (between –0.7 V and –1.3 V for 10 min to 1 h) were conducted in a one-compartment glass cell, using a fritted tube to separate the Pt mesh counter electrode in order to avoid reoxidation of CO<sub>2</sub>RR products. Long term electrochemical testing was conducted in a custom-made two-compartment cell, separated by a Nafion 117 membrane. In either cell, CO<sub>2</sub> was constantly fed into the electrolyte throughout the experiment at a flow rate of 30 mL min<sup>-1</sup>. Images and further details of each electrochemical cell can be found in Supporting Information (Figure S2, Supporting Information). The electrolysis tests comprised two steps: 1) a reductive linear sweep voltammetry (LSV) at 5 mV s<sup>-1</sup>, followed by 2) a chronoamperometry (CA) at the chosen potential for the electrolysis test, typically at –1.0 V versus RHE. The total time of chronoamperometry was set to 10 min for the typical activity tests. After 10 min, that is, at the end of the test, the headspace of the cell was sampled and analyzed by gas chromatography for H<sub>2</sub> and CO determination. In addition, a liquid sample of 1 mL was taken from the electrolyte for formate determination by <sup>1</sup>H-NMR (see details below). For long term stability tests, chronoamperometry was performed for 10 h, and the sampling for gas and liquid phase products was performed at 10 min and then at 1 h intervals.

**Reductive Cyclic Voltammetry Pretreatment:** Reductive cyclic voltammetry pretreatment was performed in the CO<sub>2</sub> bulk electrolysis cell described before (Figure S2, Supporting Information). The electrolyte was purged with N<sub>2</sub> or CO<sub>2</sub> for 15–20 min prior pre-reduction. The SnInOx samples were initially swept at 5 mV s<sup>-1</sup> from OCP to –1.2 V versus RHE and then cycled between –1.2V and –0.4 V versus RHE (2 cycles at a sweep rate of 5 mV s<sup>-1</sup> and 20 cycles at a sweep rate of 20 mV s<sup>-1</sup>). After the reductive treatment, the working electrode was kept at –0.4 V until the bulk electrolysis was started, without opening the circuit or exposing the working electrode to air to avoid film reoxidation.

**Electrolysis Test at Different Potentials:** Potential dependent electrolysis test comprised a reductive LSV at 5 mV s<sup>-1</sup> followed by a series of chronoamperometry steps at –0.7 V (1 h), –0.8 V (30 min), –0.9 V (10 min), –1.0 V (10 min), –1.1 V (10 min), –1.2 V (10 min), –1.3 V (10 min). The potential was kept at –0.4 V in between electrolysis steps to avoid reoxidation of the film at open circuit potential. At the end of

each chronoamperometry step, the headspace was sampled for gas chromatography analysis for H<sub>2</sub> and CO determination and a liquid sample of 1 mL was taken from the electrolyte for formate quantification and replaced with fresh electrolyte.

**Product Quantification:** Gas-phase products were analyzed with a GC 2014 gas chromatographer from Shimadzu. The Faradaic efficiency was calculated according to Equation (1), where Vol<sub>x</sub>% is the volume percentage of the respective gas determined by gas chromatography, flowrate corresponds to the constant inlet rate of CO<sub>2</sub> into the cell (30 mL min<sup>-1</sup>), *P* and *T* are room pressure and temperature, *z* the number of mols of electrons required to produce 1 mol of gas *X*, and *i* is the recorded experimental current.

$$\text{Faradaic Efficiency \% Gas X} = \frac{\text{Vol}_x\% \times \text{Flowrate} \times \left(\frac{P}{RT}\right) \times z \times F}{i} \times 100 \quad (1)$$

Liquid-phase products were analyzed by <sup>1</sup>H-NMR spectroscopy in a Bruker Advance III 500 MHz system with a cryoprobe detector, using a procedure adapted from a previous report.<sup>[66]</sup> Formate was the only product detected in the liquid phase. Dimethylformamide and phenol (Sigma-Aldrich) were included as internal standards with each sample. Formate faradaic efficiency was determined based on the experimentally determined formate concentration [HCOO<sup>-</sup>], the total amount of charge passed during the chronoamperometry (*q*) and the total volume of electrolyte (*V*<sub>electrolyte</sub>), as shown in Equation (2).

$$\text{Faradaic Efficiency \% HCOO}^- = \frac{[\text{HCOO}^-] \times V_{\text{electrolyte}} \times 2 \times F}{q} \times 100 \quad (2)$$

**Capacitance of SnInOx and Derivatives:** The capacitance of SnInOx films before and after CO<sub>2</sub> reduction experiments was determined electrochemically in N<sub>2</sub>-saturated 0.1 M KHCO<sub>3</sub> by cyclic voltammetry (CV). Cyclic voltammograms were recorded at different sweeping rates (between 5 and 500 mV s<sup>-1</sup>) in a potential range where no faradaic current was expected, that is, typically ±50 mV around the open-circuit voltage (OCV between 0.7–0.8 V vs RHE). The capacitive current densities at OCV (*J*<sub>anodic</sub> and *J*<sub>cathodic</sub>) were then plotted as functions of the sweeping rate. The capacitance could then be calculated as the slope of the linear relation between capacitive current density and sweeping rate, as described in Equation (3). Representative examples of this methodology are presented in Figures S9, Supporting Information.

$$J = C \frac{dV}{dt} \quad (3)$$

**Structural Characterization:** Scanning electron microscopy (SEM) images were recorded on an SEM microscope JEOL 7401F, operated at 10 kV in secondary electron imaging mode, equipped with an EDX detector Quantax 400 from Bruker. Transmission electron microscopy (TEM) images were recorded on an FEI Tecnai G<sup>2</sup> 20 S-TWIN TEM microscope operated at 200 kV, equipped with an EDAX EDX system Si(Li) SUTW detector. For TEM measurements SnInOx derived samples were scratched off the glassy carbon substrate using a scalpel and transferred onto a carbon-coated Cu-grid. EDX elemental mapping and line scan experiments were performed by HAADF-STEM microscopy on an aberration-corrected JEOL JEM-ARM200CF microscope operated at 200 kV equipped with a high angle Silicon Drift EDX detector with a solid angle of up to 0.98 steradians from a detection area of 100 mm<sup>2</sup>. GI-XRD diffraction patterns of thin films were recorded on a Bruker D8 Advance with CuKα-radiation (λ = 0.1546 nm) in grazing-incident (GI)-XRD mode with a 1° incident angle, a step size of 0.06° and a step time of 20 s. X-ray photoelectron spectroscopy measurements were performed at the ISSS beamline of the synchrotron radiation facility BESSY of the Helmholtz-Zentrum Berlin (HZB). The excitation energy was adjusted to acquire photoelectrons with 550 eV kinetic energy for all core levels (e.g., Sn3d and In3d). Depth profile information was collected with photoelectron energy adjusted to 200 and 1000 eV. The spectra were analyzed using the software Plot.

**Inert Atmosphere Transfer:** For XPS analysis samples were carefully transferred without any contact with air in order to minimize the risk of oxidation of samples surface. The samples after electrochemical pretreatment or catalytic tests were withdrawn from the electrolyte under reductive bias (–1V) in the cell. Still under bias and gas flow the samples were washed with deaerated water to remove electrolyte residues and transferred in an N<sub>2</sub>-filled Schlenk flask. Once protected in the Schlenk flask N<sub>2</sub> atmosphere, the samples were unplugged from the potentiostat and transferred into an (N<sub>2</sub>) glove box. The samples were then transferred under N<sub>2</sub> atmosphere into the XPS analysis chamber by means of a transfer arm without exposure to air.

**Inductively Coupled Plasma Optical Emission Spectrometry (ICP-OES):** The metal content of synthesized SnInOx derived catalysts was investigated by Inductively Coupled Plasma Optical Emission Spectrometry (ICP-OES) performed on a Varian ICP-OES 715 device. Sample preparation was performed by digestion of SnInOx derived thin films in a concentrated acid mixture overnight (H<sub>2</sub>SO<sub>4</sub> 98% (1 mL), HNO<sub>3</sub> 69% (1 mL), and HCl 37% (3 mL)) followed by heating at 80 °C for 1 h. After cooling to room temperature, the sample was diluted to 15 mL with Millipore water.

## Supporting Information

Supporting Information is available from the Wiley Online Library or from the author.

## Acknowledgements

Financial support was provided by the Deutsche Forschungsgemeinschaft (DFG, German Research Foundation) within the frame of the excellence Cluster UniCat (EXC 314) (A.F., M.D.) and its Berlin International Graduate School of Natural Sciences and Engineering (BIG-NSE) (L.P.P., A.G.), as well as by the German Federal Ministry of Education and Research (BMBF, grant number 03X5524 (EDELKAT) and 01FP13033F) (A.F.) and the University of Freiburg. Further support was funded by the European Union's Horizon 2020 research and innovation program (grant No. 101006701, Eco-Fuel) (P.S.). In addition, the authors would like to acknowledge the HZB for the allocation of synchrotron radiation beamtime at the ISSS beamline. Dr. Caren Göbel and Dr. Martin Rohloff are kindly acknowledged for their support with the transmission electron microscopy measurements at the ZELMI of the TU Berlin, Dr. Arno Bergmann for his support in conducting GI-XRD measurements as well as Stefan Schutte for his support in the synthesis of catalyst precursors. The NMR team lead by Dr. Sebastian Kemper at the Analytic Centre of the Institute of Chemistry at the TU Berlin is kindly acknowledged for support in formate quantification measurements.

Open access funding enabled and organized by Projekt DEAL.

## Conflict of Interest

The authors declare no conflict of interest.

## Data Availability Statement

Research data are not shared.

## Keywords

electrochemical CO<sub>2</sub> reduction, formate, indium-based electrocatalysts, metal@metal oxide core@shell electrocatalysts, oxide derived electrocatalysts, tin-based electrocatalysts

Received: April 15, 2021

Revised: June 28, 2021

Published online:

- [1] G. A. Florides, P. Christodoulides, *Environ. Int.* **2009**, *35*, 390.
- [2] D. J. Hofmann, J. H. Butler, P. P. Tans, *Atmos. Environ.* **2009**, *43*, 2084.
- [3] Mitigation of climate change: Contribution of working group III to the fourth assessment report of the Intergovernmental Panel on Climate Change, Ippc, Geneva **2007**.
- [4] C. Song, *Catal. Today* **2006**, *115*, 2.
- [5] S. Pacala, R. Socolow, *Science* **2004**, *305*, 968.
- [6] A. Heshmati, S. Abolhosseini, J. Altmann, *The Development of Renewable Energy Sources and its Significance for the Environment*, Springer, Singapore **2015**.
- [7] M. Azuma, *J. Electrochem. Soc.* **1990**, *137*, 1772.
- [8] Y. Hori, A. Murata, K. Kikuchi, S. Suzuki, *J. Chem. Soc. Chem. Commun.* **1987**, 728, <https://pubs.rsc.org/en/content/articlelanding/1987/c3/c39870000728#!divAbstract>.
- [9] Y. Hori, H. Wakebe, T. Tsukamoto, O. Koga, *Electrochim. Acta* **1994**, *39*, 1833.
- [10] S. Ikeda, T. Takagi, K. Ito, *Bull. Chem. Soc. Jpn.* **1987**, *60*, 2517.
- [11] K. Ito, S. Ikeda, N. Yamauchi, T. Iida, T. Takagi, *Bull. Chem. Soc. Jpn.* **1985**, *58*, 3027.
- [12] D. R. Kauffman, D. Alfonso, C. Matranga, H. Qian, R. Jin, *J. Am. Chem. Soc.* **2012**, *134*, 10237.
- [13] H. Noda, S. Ikeda, Y. Oda, K. Imai, M. Maeda, K. Ito, *Bull. Chem. Soc. Jpn.* **1990**, *63*, 2459.
- [14] Y. Hori, K. Kikuchi, S. Suzuki, *Chem. Lett.* **1985**, *14*, 1695.
- [15] T. Yamamoto, K. Hirota, D. A. Tryk, K. Hashimoto, A. Fujishima, M. Okawa, *Chem. Lett.* **1998**, *27*, 825.
- [16] S. Kapusta, N. Hackerman, *J. Electrochem. Soc.* **1983**, *130*, 607.
- [17] M. N. Mahmood, D. MAsheder, C. J. Harty, *J. Appl. Electrochem.* **1987**, *17*, 1159.
- [18] M. Gattrell, N. Gupta, a. Co., *J. Electroanal. Chem.* **2006**, *594*, 1.
- [19] Y. Hori, K. Kikuchi, A. Murata, S. Suzuki, *Chem. Lett.* **1986**, *15*, 897.
- [20] Y. Hori, A. Murata, R. Takahashi, *J. Chem. Soc., Faraday Trans. 1* **1989**, *85*, 2309.
- [21] J. J. Kim, D. P. Summers, K. W. Frese, M. Park, *J. Electroanal. Chem. Interfacial Electrochem.* **1988**, *245*, 223.
- [22] T. Y. Chang, R. M. Liang, P. W. Wu, J. Y. Chen, Y. C. Hsieh, *Mater. Lett.* **2009**, *63*, 1001.
- [23] I. Ganesh, *Renewable Sustainable Energy Rev.* **2014**, *31*, 221.
- [24] A. Goepfert, M. Czaun, J.-P. Jones, G. K. Surya Prakash, G. A. Olah, *Chem. Soc. Rev.* **2014**, *43*, 7995.
- [25] F. Jia, X. Yu, L. Zhang, *J. Power Sources* **2014**, *252*, 85.
- [26] J. Popić, M. Avramov-Ivić, N. Vuković, *J. Electroanal. Chem.* **1997**, *421*, 105.
- [27] Y. Hori, S. Suzuki, *Bull. Chem. Soc. Jpn.* **1982**, *55*, 660.
- [28] W. Paik, T. N. Andersen, H. Eyring, *Electrochim. Acta* **1969**, *14*, 1217.
- [29] B. J. Jordan, P. T. Smith, *Proc. Chem. Soc.* **1960**, 233.
- [30] T. E. Teeter, P. Van Rysselberghe, *J. Chem. Phys.* **1954**, *22*, 759.
- [31] K. S. Udupa, G. S. Subramanian, H. V. K. Udupa, *Electrochim. Acta* **1971**, *16*, 1593.
- [32] Y. B. Vassiliev, V. S. Bagotsky, N. V. Osetrova, O. A. Khazova, N. A. Mayorova, *J. Electroanal. Chem. Interfacial Electrochem.* **1985**, *189*, 271.
- [33] A. Dominguez-Ramos, B. Singh, X. Zhang, E. G. Hertwich, A. Irabien, *J. Cleaner Prod.* **2015**, *104*, 148.
- [34] D. T. Whipple, P. J. A. Kenis, *J. Phys. Chem. Lett.* **2010**, *1*, 3451.
- [35] I. Omae, *Catal. Today* **2006**, *115*, 33.
- [36] F. Cheng, X. Zhang, K. Mu, X. Ma, M. Jiao, Z. Wang, P. Limpachanangkul, B. Chalermisinsuwan, Y. Gao, Y. Li, Z. Chen, L. Liu, *Energy Technol.* **2021**, *9*, 2000799.
- [37] J. Li, M. Zhu, Y. F. Han, *ChemCatChem* **2021**, *13*, 514.
- [38] Y. Chen, M. W. Kanan, *J. Am. Chem. Soc.* **2012**, *134*, 1986.
- [39] D. H. Won, C. H. Choi, J. Chung, M. W. Chung, E. H. Kim, S. I. Woo, *ChemSusChem* **2015**, *8*, 3092.
- [40] S. Zhang, P. Kang, T. J. Meyer, *J. Am. Chem. Soc.* **2014**, *136*, 1734.
- [41] Z. M. Detweiler, J. L. White, S. L. Bernasek, A. B. Bocarsly, *Langmuir* **2014**, *30*, 7593.
- [42] J. L. White, A. B. Bocarsly, *J. Electrochem. Soc.* **2016**, *163*, H410.
- [43] M. F. Baruch, J. E. Pander, J. L. White, A. B. Bocarsly, *ACS Catal.* **2015**, *5*, 3148.
- [44] F. Li, H. Zhang, S. Ji, W. Liu, D. Zhang, C. Zhang, J. Yang, F. Yang, L. Lei, *Int. J. Electrochem. Sci.* **2019**, *14*, 4161.
- [45] W. J. Dong, C. J. Yoo, J. L. Lee, *ACS Appl. Mater. Interfaces* **2017**, *9*, 43575.
- [46] F. Li, L. Chen, G. P. Knowles, D. R. MacFarlane, J. Zhang, *Angew. Chem., Int. Ed.* **2017**, *56*, 505.
- [47] J. Gu, F. Héroguel, J. Luterbacher, X. Hu, *Angew. Chem., Int. Ed.* **2018**, *57*, 2943.
- [48] K. Mou, Z. Chen, S. Yao, L. Liu, *Electrochim. Acta* **2018**, *289*, 65.
- [49] L. Xiao, X. Liu, R. Zhou, T. Zhang, R. Zhou, B. Ouyang, E. Kan, P. J. Cullen, K. (Ken) Ostrikov, X. Tu, *Energy Convers. Manage.* **2021**, *231*, 113847.
- [50] J. T. Feaster, C. Shi, E. R. Cave, T. Hatsukade, D. N. Abram, K. P. Kuhl, C. Hahn, J. K. Nørskov, T. F. Jaramillo, *ACS Catal.* **2017**, *7*, 4822.
- [51] G. B. Damas, C. R. Miranda, R. Sgarbi, J. M. Portela, M. R. Camilo, F. H. B. Lima, C. M. Araujo, *Catalysts* **2019**, *9*, 636.
- [52] A. Dutta, A. Kuzume, V. Kaliginedi, M. Rahaman, I. Sinev, M. Ahmadi, B. Roldán Cuenya, S. Vesztergom, P. Broekmann, *Nano Energy* **2018**, *53*, 828.
- [53] A. Guiet, C. Göbel, K. Klingan, M. Lublow, T. Reier, U. Vainio, R. Kraehnert, H. Schlaad, P. Strasser, I. Zaharieva, H. Dau, M. Driess, J. Polte, A. Fischer, *Adv. Funct. Mater.* **2015**, *25*, 6228.
- [54] A. Guiet, T. Reier, N. Heidary, D. Felkel, B. Johnson, U. Vainio, H. Schlaad, Y. Aksu, M. Driess, P. Strasser, A. Thomas, J. Polte, A. Fischer, *Chem. Mater.* **2013**, *25*, 4645.
- [55] A. Guiet, T. Unmüßig, C. Göbel, U. Vainio, M. Wollgarten, M. Driess, H. Schlaad, J. Polte, A. Fischer, *ACS Appl. Mater. Interfaces* **2016**, *8*, 28019.
- [56] Y. Aksu, M. Driess, *Angew. Chem., Int. Ed.* **2009**, *48*, 7778.
- [57] G. O. Larrazábal, A. J. Martín, S. Mitchell, R. Hauert, J. Pérez-Ramírez, *ACS Catal.* **2016**, *6*, 6265.
- [58] Y. Yang, C. Tan, Y. Yang, L. Zhang, B. Zhang, K. Wu, S. Zhao, *ChemCatChem* **2021**, *13*, 1587.
- [59] S.-I. Choi, M. Shao, N. Lu, A. Ruditskiy, H.-C. Peng, J. Park, S. Guerrero, J. Wang, M. J. Kim, Y. Xia, *ACS Nano* **2014**, *8*, 10363.
- [60] W. Luc, C. Collins, S. Wang, H. Xin, K. He, Y. Kang, F. Jiao, *J. Am. Chem. Soc.* **2017**, *139*, 1885.
- [61] Z. Cai, Y. Wu, Z. Wu, L. Yin, Z. Weng, Y. Zhong, W. Xu, X. Sun, H. Wang, *ACS Energy Lett.* **2018**, *3*, 2816.
- [62] S. Tanuma, D. R. Penn, *Surf. Interface Anal.* **1992**, *20*, 77.
- [63] C. Donley, D. Dunphy, D. Paine, C. Carter, K. Nebesny, P. Lee, D. Alloway, N. R. Armstrong, *Langmuir* **2002**, *18*, 450.
- [64] Y. G. Kim, J. H. Baricuatro, A. Javier, J. M. Gregoire, M. P. Soriaga, *Langmuir* **2014**, *30*, 15053.
- [65] Y. Liu, A. Z. Fire, S. Boyd, R. A. Olshen, *Proc. Natl. Acad. Sci. U. S. A.* **2014**, *114*, 5918.
- [66] K. P. Kuhl, E. R. Cave, D. N. Abram, T. F. Jaramillo, *Energy Environ. Sci.* **2012**, *5*, 7050.